

**Subcontract XAT-4-33624-01**

**“Development of a Wide Band Gap Cell for Thin Film Tandem Solar Cells”**

**3rd Quarterly Report**

**to**

**National Renewable Energy Laboratory**

**From**

**Institute of Energy Conversion  
University of Delaware**

**For period 5/6/04 - 8/5/04**

**Task 1: I-III-VI<sub>2</sub>-based Solar Cells**

*Cu(InGa)(SeS)<sub>2</sub> Film Growth*

In the last quarterly report, we discussed the relative incorporation of S and Se during CuIn(SeS)<sub>2</sub> or Cu(InGa)(SeS)<sub>2</sub> film deposition. It was shown that the relative S/(Se+S) incorporation depends on Cu/In or Cu/(In+Ga). For Cu/(In+Ga) larger than about 1.05 (Cu-rich), S/(Se+S) in the film is greater than in the flux during deposition. For Cu/(In+Ga) less than about 0.90 (Cu-poor), Se is preferentially incorporated. For Cu/(In+Ga) between 0.9 and 1.0, there is a steep dependence of S/(Se+S) in the film versus Cu/(In+Ga). Further analysis of the relative S/(Se+S) incorporation is focusing on CuIn(SeS)<sub>2</sub> films with varying Cu/In and S/(Se+S) ratios during deposition. The absence of Ga facilitates quantitative analysis of X-ray diffraction (XRD) or optical data because there are unique solutions to the composition dependence of lattice parameter or bandgap.

A single CuIn(SeS)<sub>2</sub> run, #24133, was deposited with a gradient in Cu/In from 0.85 to 1.1 across the 3” x 3” substrate array. For this run, the flux had S/(Se+S) = 0.71 and S/(Se+S) in the films varied from 0.33 to 0.78 as Cu/(In+Ga) increased, as shown in the previous report. For Cu-rich films from this run, the XRD spectra indicate a single chalcopyrite composition with peaks at 2θ values consistent with the film composition determined by energy dispersive X-ray spectroscopy (EDS). On the other hand, XRD spectra for the Cu-poor samples from this run show doublets indicating 2 distinct chalcopyrite compositions. For example, Figure 1 shows the XRD spectrum from a sample with Cu/In = 0.87, and S/(S+Se) = 0.34. Peaks 1, 2, and 3 at lower 2θ can be assigned to a composition of CuIn(S<sub>0.7</sub>Se<sub>0.3</sub>)<sub>2</sub> and peaks a, b, and c at higher 2θ to a composition of CuIn(S<sub>0.2</sub>Se<sub>0.8</sub>)<sub>2</sub>.

Glancing incidence X-ray diffraction (GIXRD) angle spectra were measured on the same Cu-poor film at 5 different incidence angles. Figure 2 shows the spectra near the (112) peak normalized to the low  $2\theta$  peak. The peak at higher  $2\theta$ , corresponding to greater S, only emerges from the noise at a  $2.5^\circ$  incident angle which samples a depth of approximately 550 nm. It is, therefore, apparent that the film has a roughly bilayer structure with more Se-rich material closer to the surface of the film and more S-rich material nearer to the Mo. This result was surprising since the elemental flux from the sources was intended to be constant throughout the run. Indeed, the total flux, as measured by a quartz crystal monitor, had a constant rate throughout the run.

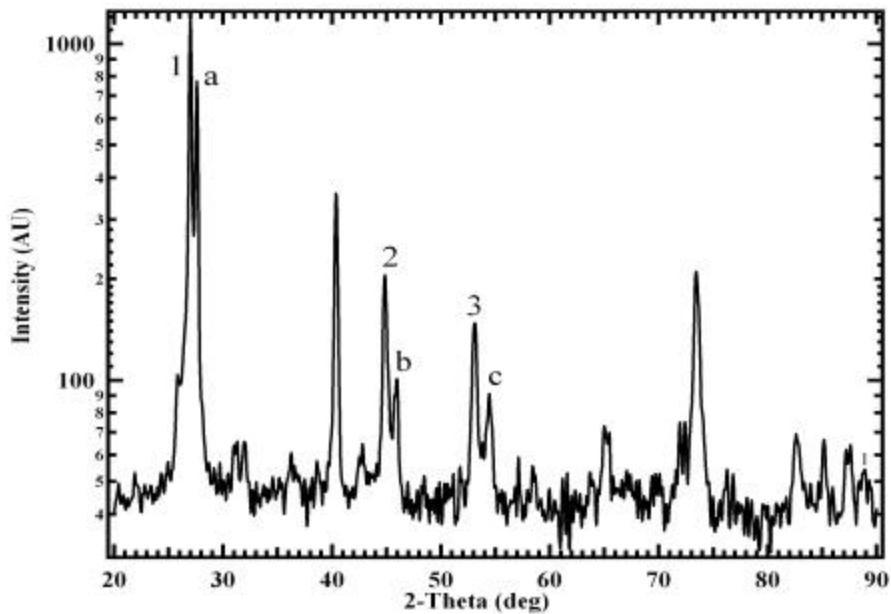


Figure 1. XRD scan for film from run 24133 with  $\text{Cu/In} = 0.87$  and  $\text{S}/(\text{Se}+\text{S}) = 0.34$ . Peaks 1, 2, and 3 are reflections from a different chalcopyrite composition than peaks a, b, and c.

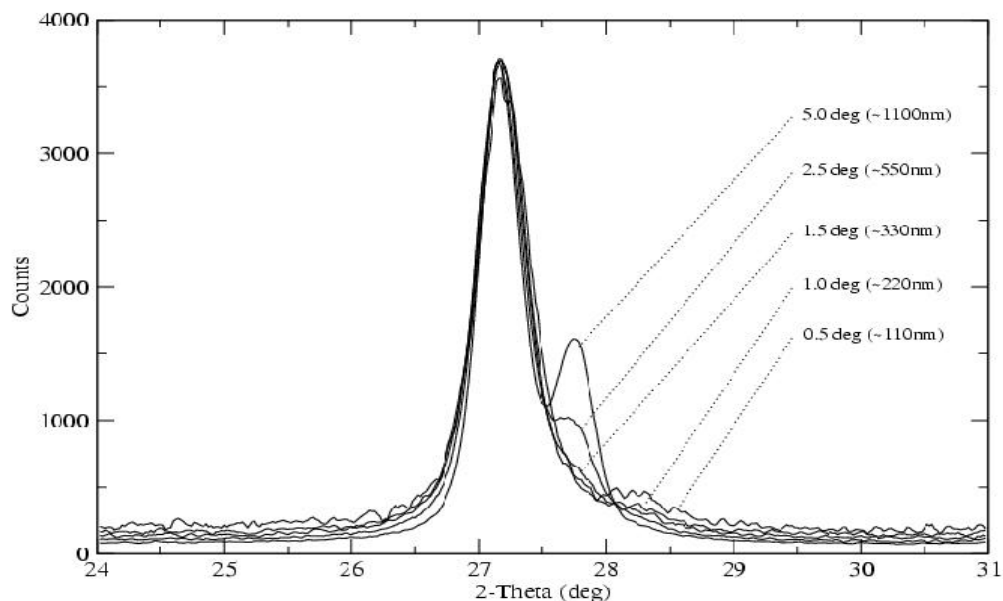


Figure 2. Normalized GIXRD of the (112) doublet at different incidence angles and sampling depths of the same film shown in Figure 1.

To further study this apparent vertical composition segregation, Auger electron spectroscopy (AES) depth profiling was performed at National Renewable Energy Laboratory (NREL). The through-film composition is shown in Figure 3 for a film with Cu/In = 0.9 as measured by EDS with 20 kV accelerating voltage. It should be noted that the EDS measurement determines the composition over roughly the top half of the film. This AES data shows a Se-rich layer near the surface, and a S-rich layer, with higher Cu content underneath. This is consistent with the GIXRD data. An AES depth profile of a Cu-rich film showed relatively flat S and Se profiles and a  $\text{Cu}(\text{SeS})_x$  layer in the near surface region.

To test whether the chalcopyrite bilayer results from unintentional variation in the source fluxes, a  $\text{CuIn}(\text{SeS})_2$  run (# 24141) was done with a change in Cu/In ratio from Cu-poor to Cu-rich halfway through. Thus, in the absence of diffusion, the films might be expected to be layered opposite to the Cu-poor samples discussed above, if the film preferentially incorporates Se during the Cu-poor growth and S when the flux contains excess Cu. EDS measurements of the resulting films gave Cu/In = 0.94 and XRD scans again indicated two different chalcopyrite compositions. GIXRD measurements (Figure 4) indicate that the intensity ratio of the S-rich (112) peak to the Se-rich (112) peak increases with increasing glancing angle. So, the S-rich chalcopyrite phase is preferentially located near the substrate, just as it was when source fluxes were intentionally kept constant throughout the growth. Thus, it seems that the phase composition and layering of Cu-poor films is a result of kinetic and/or thermodynamic factors during film growth rather than being directly related to changes in flux from the sources during growth.

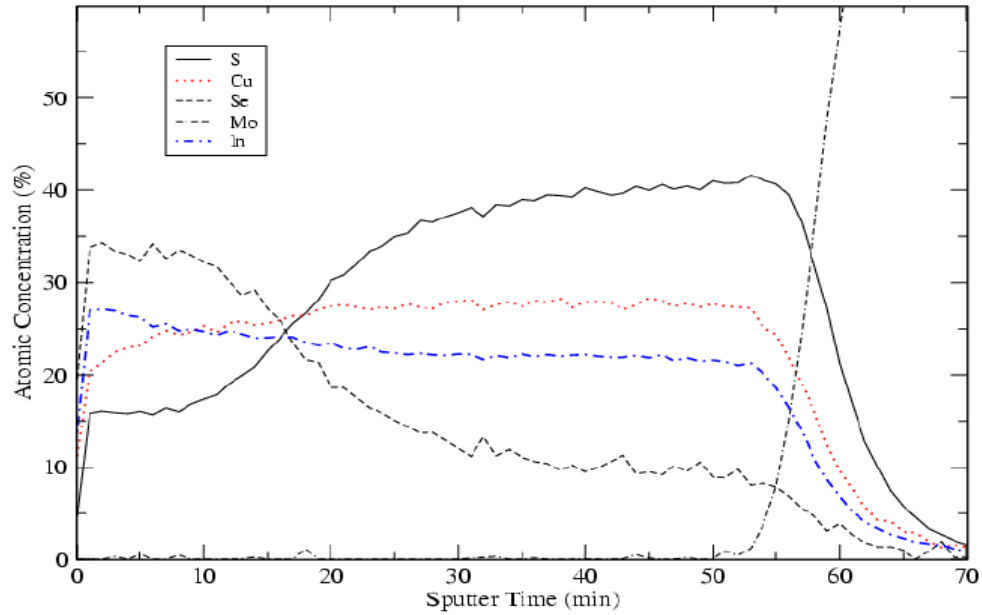


Figure 3. AES depth profile of a bi-layer  $\text{CuIn}(\text{SeS})_2$  film from run 24133.

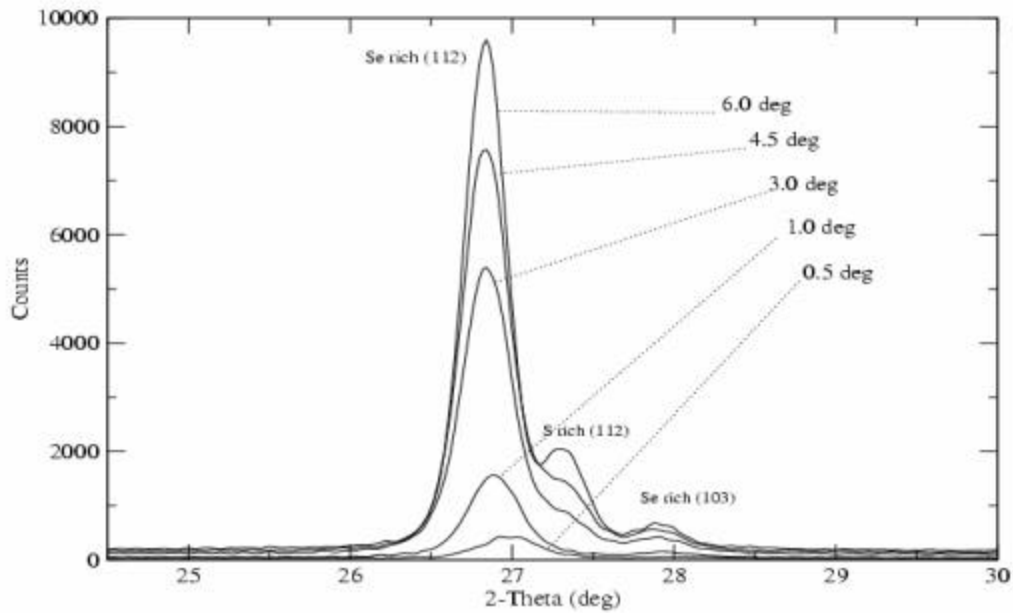


Figure 4. GIXRD of film deposited with a change from Cu-poor to Cu-rich flux during growth.

The formation of chalcopyrite phases of two different compositions during ostensibly constant flux film growth raises the possibility that there may be a miscibility gap in the phase diagram for this system that has, to our knowledge, not been previously reported. A miscibility gap between the sulfide and telluride chalcopyrite alloys has been reported [1], but the same study found that  $\text{CuInSe}_2$  and  $\text{CuInS}_2$  were miscible in all chalcogen

proportions. Cu and In were not systematically varied or specified in that study, however. We are presently planning depositions with varying substrate temperatures, growth times, and incident fluxes to attempt to determine if there is a miscibility gap and to understand more about the growth mechanism.

### *Cu(InGa)(SeS)<sub>2</sub> Devices*

Previous comparison, shown in the last monthly report, of Cu(InGa)Se<sub>2</sub> and CuInS<sub>2</sub> showed lower V<sub>oc</sub> but higher J<sub>sc</sub> and better long wavelength collection in the CuInS<sub>2</sub> cell. To better understand the difference in the current collection, as seen in quantum efficiency measurements, in-depth optical characterization of a CuInS<sub>2</sub> film has been completed, using spectroscopic ellipsometry (SE). Preparation of the films, details of the measurement, and the optical model used to determine optical constants n and k, were the same as described for Cu(InGa)Se<sub>2</sub> films [2]. The film characterized was a CuInS<sub>2</sub> film that was deposited with Cu-rich composition and then KCN etched, the same procedure used to produce the highest efficiency devices. To obtain a surface sufficiently smooth for analysis of the SE data, the sample was peeled from the Mo-coated glass substrate.

The complete optical characterization included determination of the optical constants over the energy range 0.8 = E = 4.6 eV. However, the value of k is very close to 0 in the transparent sub-bandgap region and, therefore, the absorption coefficient  $\alpha = 4\pi k/\lambda$  has greater uncertainty in this range. Figure 5 shows the wavelength dependence of  $\alpha$  over the range of interest for solar cell operation. This is compared to  $\alpha$  for Cu(InGa)Se<sub>2</sub> with E<sub>g</sub> = 1.53 eV corresponding to Ga/(In+Ga) = 0.83. The latter was determined by interpolating between the data in reference 2 for films with E<sub>g</sub> = 1.37 and 1.69 eV.

The CuInS<sub>2</sub> film has higher absorption coefficient with the difference increasing at longer wavelength, closer to the bandgap. SE measurements of single crystals also showed a higher  $\alpha$  for CuInS<sub>2</sub> than for Cu(InGa)Se<sub>2</sub> [3,4]. Thus, higher absorption coefficient could account for higher quantum efficiency. To model the QE based on the measured  $\alpha$  data requires a collection length in the simplest case, or, to be more precise, a minority carrier diffusion length and space charge width. The latter will be determined independently from capacitance measurements before such a model is developed.

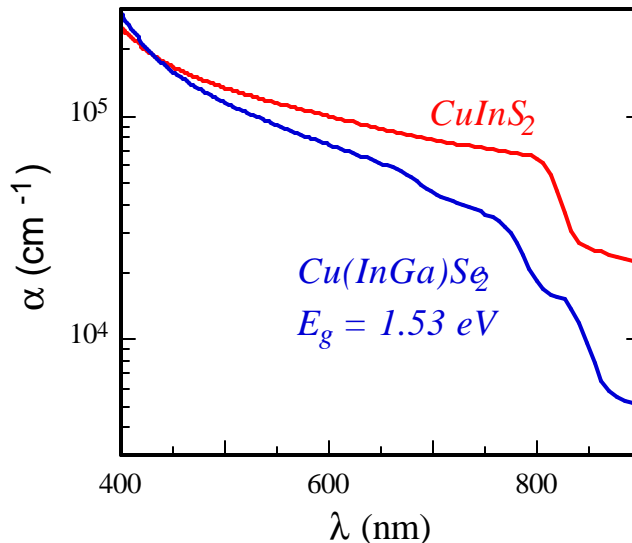


Figure 5. Absorption coefficients of  $\text{CuInS}_2$  and  $\text{Cu(InGa)Se}_2$  ( $E_g = 1.53 \text{ eV}$ ) determined from SE analysis of evaporated thin films.

The difference between the  $\text{Cu(InGa)Se}_2$  and  $\text{CuInS}_2$  devices is reminiscent of the behavior seen in  $\text{CuInSe}_2$  devices after oxidizing and reducing treatments, respectively with higher  $V_{oc}$  but poorer long wavelength collection observed after annealing in an oxygen containing atmosphere [5,6]. This was attributed to increased conductivity of the  $\text{CuInSe}_2$ . Consequently, experiments were done to study the effect of the oxidation of the  $\text{CuInS}_2$  and determine if this could be used to increase the low  $V_{oc}$ . Previously, we have found that completed solar cells showed little or no increase in  $V_{oc}$  with air annealing at  $200^\circ\text{C}$ . In the present experiments,  $\text{CuInS}_2$  films were oxidized either by air annealing or by chemical treatment in  $\text{H}_2\text{O}_2$ . Devices were then fabricated using the baseline processes including CBD CdS. As the results in Table 1 show, there was no increase in  $V_{oc}$  or cell efficiency with these treatments.  $V_{oc}$  fell within the same range as the control samples with no treatment.

Table 1. CuInS<sub>2</sub> device results with oxidizing treatments of the CuInS<sub>2</sub> film. All films were from a single Cu-rich deposition and were etched in KCN.

#	treatment before CdS		Eff (%)	V <sub>oc</sub> (Volts)	J <sub>sc</sub> (mA/cm <sup>2</sup> )	FF (%)	R <sub>oc</sub> (Ω-cm <sup>2</sup> )	G <sub>sc</sub> (mS/cm <sup>2</sup> )
32	-	Best	8.0	0.633	20.1	62.9	3.3	3
		Avg	7.7	0.629	19.1	63.8	3.2	3
12	-	Best	6.6	0.584	21.2	53.1	4.4	8
		Avg	5.6	0.561	18.7	53.2	5.2	7
13	air anneal (30m, 200°C)	Best	6.9	0.588	20.0	58.7	4.0	3
		Avg	6.4	0.566	20.0	56.1	4.4	5
22	1% H <sub>2</sub> O <sub>2</sub> (1 m)	Best	8.2	0.654	20.2	62.4	3.6	3
		Avg	7.5	0.642	19.8	59.3	3.8	4
33	0.1% H <sub>2</sub> O <sub>2</sub> (1 m)	Best	7.9	0.630	21.2	58.9	3.4	4
		Avg	7.1	0.621	20.9	54.5	3.9	6

## Task 2. II-VI-based Solar Cells

Effort focused on analysis and development of post-deposition treatments and quantification of the CdS-Cd<sub>1-x</sub>Zn<sub>x</sub>Te interface chemistry under conditions used to fabricate cells. This report presents materials analysis and device results for CdS/Cd<sub>1-x</sub>Zn<sub>x</sub>Te structures treated at ~400°C in chloride vapor.

### *CdS-Cd<sub>1-x</sub>Zn<sub>x</sub>Te Interface Chemistry*

CdS/Cd<sub>1-x</sub>Zn<sub>x</sub>Te samples from a single deposition (T<sub>dep</sub> = 325°C) were annealed in argon, then treated in different chloride ambients, consisting of either ZnCl<sub>2</sub>, CdCl<sub>2</sub>, or mixed CdCl<sub>2</sub> + ZnCl<sub>2</sub> vapor (abbreviated ZnCdCl<sub>2</sub>), achieved by mixing equal quantities of CdCl<sub>2</sub> and ZnCl<sub>2</sub> in the source susceptor of the treatment reactor. The ZnCl<sub>2</sub> and CdCl<sub>2</sub> source temperatures were selected from previous experiments, shown to activate CdTe/CdS junctions. For the mixed source, an intermediate temperature was selected (Table 2).

Table 2. Source temperatures and expected partial pressures for chloride vapor treatments.

Chloride	T (°C)	P <sub>sat</sub> (mTorr)
ZnCl <sub>2</sub>	305	11
CdCl <sub>2</sub>	400	4
(ZnCd)Cl <sub>2</sub>	380	320 (ZnCl <sub>2</sub> ) 1 (CdCl <sub>2</sub> )

The treatments were 30 minutes in duration and were carried out at low oxygen partial pressure,  $pO_2 < 1$  Torr, to minimize ZnO formation. Wide-angle symmetric XRD analysis (Cu- $k\alpha$ ) was performed to determine final phase composition using the bulk lattice parameter. The bulk lattice parameter was determined by extrapolation of (hkl) lattice parameters on a Nelson-Riley-Sinclair-Taylor (NRST) plot. Detailed scans of the (511)/(333) plane ( $2\theta \sim 77^\circ$ ) were made to determine the lattice parameter distribution in the bulk of the film. At the incident beam angle ( $\theta = 38.5^\circ$ ), the Cu- $k\alpha$  x-ray diffraction sampling depth is approximately 2.5  $\mu\text{m}$ . Given the film thickness is  $\sim 3\text{-}4$   $\mu\text{m}$ , the lower half of the  $\text{Cd}_{1-x}\text{Zn}_x\text{Te}$  film and the underlying CdS/TCO films are not detected.

The treatment conditions and results are summarized in Table 3. The 600°C argon anneal improved film crystallinity and increased the lattice parameter slightly, corresponding to a reduction in x in  $\text{Cd}_{1-x}\text{Zn}_x\text{Te}$ . The treatment in  $\text{ZnCl}_2$  ambient produced no other change in the film, while the treatment in  $\text{CdCl}_2$  ambient increased the lattice parameter to near that of pure CdTe (6.481Å). The treatment in mixed ambient also increased the lattice parameter, but broadened the peaks, indicating a wide Zn composition range within the film. That the film did not convert completely to CdTe is attributed to the low  $\text{CdCl}_2$  partial pressure compared to the sample treated in  $\text{CdCl}_2$  ambient, thereby slowing the driving force for the exchange between lattice-bound Zn and Cd vapor.

Table 3. Post deposition treatments and results of XRD and visible analysis. Bulk composition (x) is estimated from the lattice parameter, determined by extrapolation on a NRST plot.

Sample	Argon Anneal 600°C	Vapor Treat 400°C	Lattice Parameter Å $\pm 0.005$	x $\pm 0.01$	Comment
41140.13	N	N	6.338	0.38	Single XRD peaks
41140.23	Y	N	6.350	0.35	Sharp singlet XRD peaks
41140.23	Y	$\text{ZnCl}_2$	6.350	0.35	Singlet XRD Peaks
41140.12	Y	$\text{ZnCdCl}_2$	6.469	0.03	Peaks broadened, degraded CdS
41140.13	Y	$\text{CdCl}_2$	6.480	0.00	Singlet XRD peaks, degraded CdS

Optically viewing the samples through the glass-side, however, revealed the integrity of the CdS- $\text{Cd}_{1-x}\text{Zn}_x\text{Te}$  interface, and in some cases, it was possible to delaminate the film from the TCO and mount it on a glass substrate for analysis of the junction-side of the structure. Viewing the samples through the glass side showed a noticeable change in appearance of the films treated in either  $\text{CdCl}_2$  or mixed chloride ambient, suggesting degradation in the CdS film. To analyze this side of the device more completely, film 41110.12, treated in mixed ambient, was delaminated from the original substrate by bonding to a glass support. The film stack separated at the ITO-CdS interface. Wide angle and narrow angle XRD analyses were performed before delamination from the  $\text{Cd}_{1-x}\text{Zn}_x\text{Te}$  (back) side and after delamination from the CdS (front) side and are shown in Figure 6.

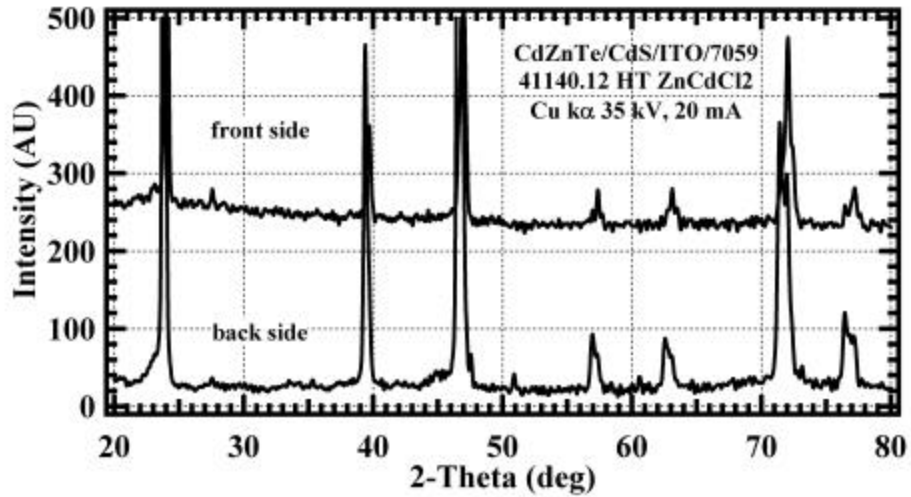


Figure 6. XRD of CdS/Cd<sub>1-x</sub>Zn<sub>x</sub>Te after treatment in mixed chloride ambient: sample 41140-11.

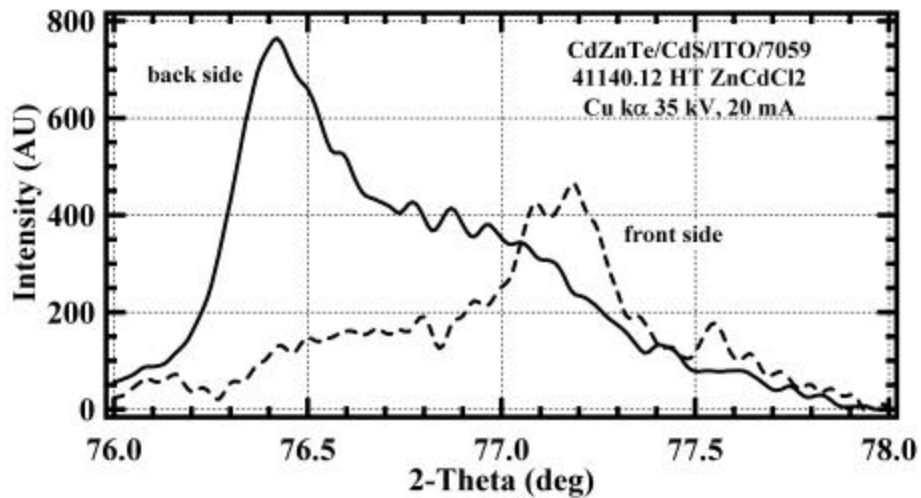


Figure 7. XRD of (511)/(333) peak after treatment in mixed chloride ambient: sample 41140-11.

In Figure 6, the majority peaks are due to the Cd<sub>1-x</sub>Zn<sub>x</sub>Te alloy and are shifted to lower Bragg angle for the backside measurement, indicating a through-film gradient in Zn concentration (less Zn at the back surface after treatment). This is seen in more detail for the (511)/(333) peak in Figure 7. The difference in peak area and intensity between the two measurements is due to differing specimen area, which is smaller for the delaminated (front-side) case.

On the wide angle back-side measurement, minor peaks are detected at 27.55°, 33.5°, 35.3°, 50.9°, and 60.6°. Of these, all but the first are ITO, originating from the exposed edge of the sample. No CdS peaks are found on either pattern, even though the initial

CdS film was ~200 nm thick. Furthermore, no oxide peaks were found, indicating good control over the oxygen concentration in the ambient during the treatments. Both patterns exhibit a minor peak at  $27.55^\circ$  ( $d = 3.235 \text{ \AA}$ ) which exhibits low crystallinity from the back and good crystallinity and intensity from the front. This peak is interpreted as being the wurtzite basal plane, (002), for  $\text{Cd}_{1-x}\text{Zn}_x\text{S}$  with  $x \sim 0.5$ . Thus, the mixed ambient treatment removed Zn from the lattice at the back surface, while CdS reacted with either the  $\text{Cd}_{1-x}\text{Zn}_x\text{Te}$  film or with  $\text{ZnCl}_2$  to form  $\text{Cd}_{1-x}\text{Zn}_x\text{S}$ . Either way, this measurement confirms that interface diffusion and reaction occur during the  $\text{ZnCl}_2$  treatment. Our prior understanding of CdS/CdTe devices shows that such reactions are kinetically limited by diffusion, with the grain boundaries providing the diffusion-enhancing pathways for intermixing [7]. In the present CdS-  $\text{Cd}_{1-x}\text{Zn}_x\text{Te}$  system, the driving force for this process is the large formation enthalpy for ZnS (-48 kcal/mol).

### *Cd<sub>1-x</sub>Zn<sub>x</sub>Te Devices*

To determine the effect of the CdS window layer on device operation, cells were made with and without CdS and processed with different halide ambient compositions. The cell structures were fabricated on  $\text{SnO}_2$ -coated borosilicate glass provided by R. Dhere at NREL. The post-deposition process consisted of: 1) anneal in argon at  $550^\circ\text{C}$  for 25 minutes; 2) treatment at  $410^\circ\text{C}$  in  $\text{ZnCl}_2$  vapor or  $\text{ZnCl}_2+\text{CdCl}_2$  vapor, with  $p(\text{O}_2) < 5 \text{ m Torr}$ ; 3) surface etching to form Te layer; 4) deposition of Cu layer, followed by thermal anneal at  $180^\circ\text{C}$  for 30 min; and application of graphite paste contact. Since treatments in  $\text{CdCl}_2$  ambient convert alloy films to pure CdTe, no effort was made to fabricate devices in  $\text{CdCl}_2$  vapor. Device results are summarized in Table 4.

Table 4. Device results for cells with and without CdS, at different  $\text{Cd}_{1-x}\text{Zn}_x\text{Te}$  starting composition.

Sample	x	E <sub>g</sub> (eV)	CdS?	HT	J <sub>sc</sub> (mA/cm <sup>2</sup> )	V <sub>oc</sub> (mV)
41188.22	0.05	1.53	N	ZnCl <sub>2</sub>	6.4	85
41188.21	0.05	1.53	N	ZnCdCl <sub>2</sub>	7.3	89
41183.11	0.05	1.53	Y	ZnCl <sub>2</sub>	19.5	734
41189.22	0.10	1.56	Y	ZnCl <sub>2</sub>	0.2	152
41189.23	0.10	1.56	Y	ZnCdCl <sub>2</sub>	4.1	386
41194.12	0.20	1.62	N	ZnCl <sub>2</sub>	8.1	138
41194.13	0.20	1.62	N	ZnCdCl <sub>2</sub>	8.1	194
41190.22	0.20	1.62	Y	ZnCl <sub>2</sub>	0.3	434
41190.23	0.20	1.62	Y	ZnCdCl <sub>2</sub>	1.0	376

For samples with low Zn content,  $x = 0.05$ , reasonable J<sub>sc</sub> and V<sub>oc</sub> were obtained for the sample with CdS window layer using  $\text{ZnCl}_2$  treatment. In fact, the cell behavior is similar to that obtained for PVD CdS/CdTe cells treated with  $\text{ZnCl}_2$  (41167.11: V<sub>oc</sub> = 650 mV; J<sub>sc</sub> = 25 mA/cm<sup>2</sup>; FF = 52%). Without CdS, both junction quality and current collection are poor. For samples with  $x \sim 0.2$ , similar device results were obtained for

treatment in  $\text{ZnCl}_2$  and in mixed  $\text{ZnCdCl}_2$ , but the presence of the CdS layer significantly limited  $J_{sc}$ . The J-V behavior and QE for cell 41194.12, processed without CdS and with  $\text{ZnCl}_2$  vapor, are shown in Figures 8 and 9.

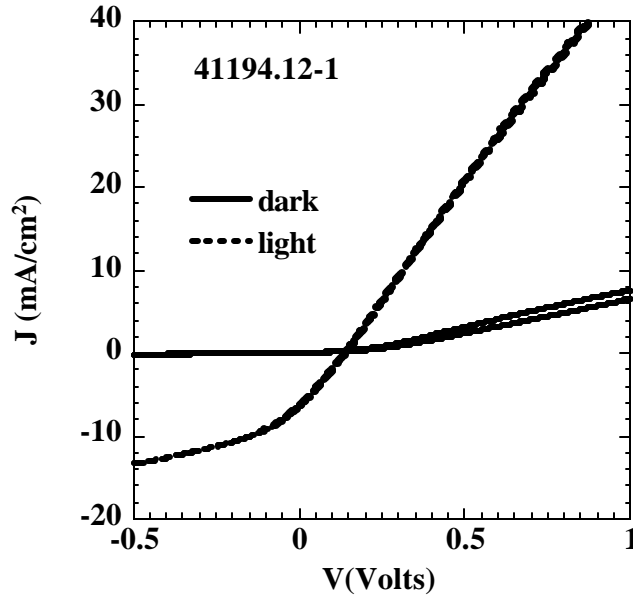


Figure 8. Dark and light J-V behavior of  $\text{SnO}_2/\text{Cd}_{1-x}\text{Zn}_x\text{Te}$  ( $x = 0.2$ ): 41194-12.

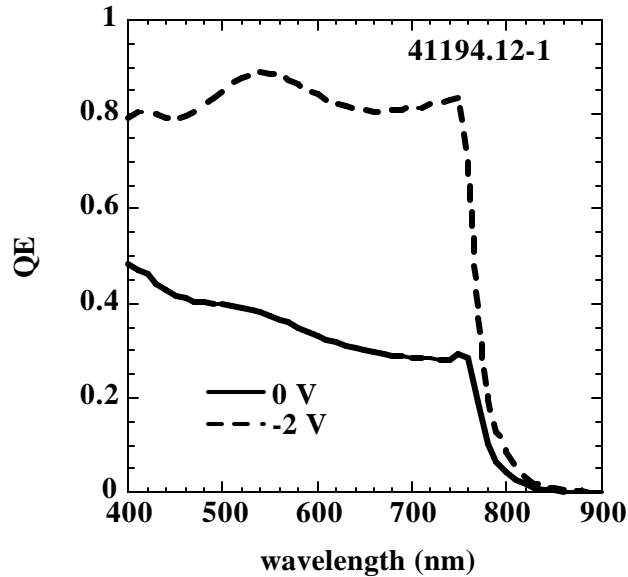


Figure 9. QE with light bias, at 0V and -2 V, for the cell of Figure 8.

The dark J-V curve of Figure 8 indicates diode behavior limited by series resistance. The light curve is limited by collection, and the light generated current saturates at -2V (reverse bias) giving  $J_L = 19.3 \text{ mA/cm}^2$ . This increase in  $J_L$  with reverse bias is clearly evident in Figure 9, which compares the QE at 0V and at -2V. At 0V, the collection peak

is at short wavelength. Both  $J_{sc}$  and  $J_L$  of this device exceed those values obtained for the devices fabricated with CdS/SnO<sub>2</sub> window layers. The  $V_{oc}$  of the device is extremely low but is comparable to  $V_{oc}$  obtained on CdTe/SnO<sub>2</sub> devices fabricated with no high resistance layer.

In summary, for devices with  $x \sim 0.2$  ( $E_g \sim 1.6$  eV) processed with SnO<sub>2</sub> window layer, a CdS heteropartner yields higher  $V_{oc}$  but severely limits  $J_{sc}$ , which the work above suggests is due to CdS- Cd<sub>1-x</sub>Zn<sub>x</sub>Te interaction. Both poor bulk transport in Cd<sub>1-x</sub>Zn<sub>x</sub>Te and chemical reactivity may be linked to as-deposited film properties associated with low-temperature (325°C) deposition. Two options are being examined to follow-up this: 1) depositing at higher temperature using vapor transport deposition, which yielded promising results during Phase Ib and 2) utilizing a cap layer to retard chloride penetration and Zn loss and allow the use of CdCl<sub>2</sub>, which yields higher performance in CdS/CdTe cells.

### **Task III: Collaboration**

Cu(InGa)Se<sub>2</sub> films were deposited with semi-transparent, ~ 40 nm thick, Mo back contacts that allow partial illumination of the Cu(InGa)Se<sub>2</sub> through the back contact for characterization at the University of Oregon. Cu(InGa)Se<sub>2</sub> runs were done with 2 relative Ga concentrations to give  $E_g = 1.2$  and  $1.5$  eV and devices were completed. The devices with the thin Mo were comparable to control samples from the same runs with standard, 0.7 μm thick, Mo except for increased series resistance. At University of Oregon, above-bandgap light will be used to generate carriers near the semitransparent back contact, resulting in the propagation of electron carriers toward the top surface. By modulating this light at very high frequencies, the current response will be analyzed to determine if minority carrier mobilities can be determined.

Also, a sample with CuInS<sub>2</sub> solar cells was provided to U. Oregon for characterization of defect concentrations and transport properties using techniques including transient photocapacitance and drive level capacitance. The results will be compared to previously reported results on Cu(InGa)Se<sub>2</sub> devices.

### **Publications**

A paper entitled “Five Source PVD For The Deposition Of Cu(In<sub>1-x</sub>Ga<sub>x</sub>)(Se<sub>1-y</sub>S<sub>y</sub>)<sub>2</sub> Absorber Layers” by Mario Gossila and William Shafarman was presented at the EMRS Spring Meeting in Strasbourg, FR and then accepted for publication in *Thin Solid Films*. A copy is attached. In addition, a paper entitled “The Determination Of Carrier Mobilities In CIGS Photovoltaic Devices Using High Frequency Admittance Measurements” by JinWoo Lee, J. David Cohen, and William N. Shafarman was presented at the same EMRS meeting and was also accepted for publication in *Thin Solid Films*.

1. J.E. Avon, K. Yooder, and J.C. Woolee, *J. Appl Phys.* **52**, 524 (1984).
2. P.D. Paulson, R.W. Birkmire, and W.N. Shafarman, *J. Appl Phys.* **94**, 879 (2003).
3. M.I. Alonso, K. Wakita, J. Pascual, M. Garriga and N. Yamamoto, *Phys. Rev. B* **63**, 075203 (2001).
4. M.I. Alonso, M. Garriga, C.A. Durante Rincón, E. Hernández and M. León, *Appl. Phys. A* **74**, 659, (2002).
5. M. Roy and J.E. Phillips, Proc. 21st IEEE PVSC, 743 (1990).
6. R. Noufi, R.J. Matson, R.C. Powell and C. Herrington, *Solar Cells* **16**, 479 (1986).
7. B.E. McCandless, M.G. Engelmann, R.W. Birkmire, *J. Appl. Phys.* **89**, 988 (2001).